Twist-tunable moiré optical resonances

Natalia S. Salakhova [1,*] Ilia M. Fradkin [1,2] Sergey A. Dyakov [1] and Nikolay A. Gippius[1]

[1]*Skolkovo Institute of Science and Technology, Bolshoy Boulevard 30, bld. 1, Moscow 121205, Russia*
[2]*Moscow Institute of Physics and Technology, Institutskiy pereulok 9, Moscow Region 141701, Russia*

Multilayer stacks of twisted optical metasurfaces are considered as a prospective platform for chiral nanophotonic devices. Such structures are primarily used for the realization of circularly polarized light sources, artificial optical rotation, and circular dichroism. At the same time, the behavior of their hybrid photonic modes is strongly affected by the moiré pattern of superimposed periodic constituents. In this paper, we show that moiré periodicity in bilayer dielectric photonic crystal slabs (PCSs) leads to a rise of unlimitedly narrow optical resonances, which are very sensitive to the relative twist and gap width between the sublayers. We demonstrate the structure providing twist-tuning of the hybrid mode wavelength in the range of 300–600 nm with the quality factor varying from 10^2 up to 10^5 correspondingly. The obtained results pave the way for the utilization of moiré-assisted effects in multilayer PCSs.

I. INTRODUCTION

Optical metasurfaces and photonic crystal slabs (PCSs) represent a notable branch of modern nanophotonics. They underlie a plethora of devices designed over the past several decades for the purposes of sensing [1–5], resonant field enhancement [6–8], second or third harmonics generation [9–12], nanolasing [13–16], on-chip light manipulation [17,18], holography [19–22], flat optics [23–25], etc. One of the ways to enrich the available options of the already diversified world of periodic optical structures is to introduce the hybridization of their modes. This concept includes lattices with complex unit cells [26–29], plasmon-photonic structures [18,30], and stacks of metasurfaces [31–37]. In an attempt to find ways to engineer structures with desired optical properties, the famous concept of twistronics [38–48] was applied in purely optical devices as well. Twisted stacks are primarily known as chiral structures for efficient interaction with circularly polarized light [49–55], but their potential is much wider. Recent studies have demonstrated rich opportunities for dispersion control in twisted bilayers of two-dimensional (2D) materials and topological transitions [54,56–62], light localization [63–69], development of tunable optical devices [53–55,70–73], engineering of peculiar photonic modes and bands [74–81], and some other purposes [82,83].

Moreover, the relative rotation of periodic structures leads to the appearance of a superlattice [54], which is associated with widely known moiré patterns. As we demonstrated in our previous paper [54], the interaction between the lattices results in the excitation of not only the diffraction harmonics of each sublattice but also the hybrid, moiré-induced ones. In turn, these harmonics lead to the rise of some peculiar moiré modes that require detailed analysis.

Here, we study the interaction of two twisted PCSs sketched in Fig. 1. Being equipped with our domestically developed moiré-adapted Fourier modal method (MA-FMM) [54], we calculate spectral maps of the twisted structures and demonstrate extremely narrow mechanically tunable moiré-induced modes. We show that these hybrid modes are highly sensitive to the rotation of sublayers and the distance between them. We achieve a twofold spectral shift of the mode wavelength (between 300 and 600 nm) and quality factor variation in the range from 10^2 to 10^5. Our results pave the way for the practical engineering of twisted metasurfaces with high-quality, tunable optical modes for modern nanophotonics.

II. RESULTS

In this paper, we consider the structure of two identical lamellar PCSs. Figure 1 shows the vacuum-surrounded lattices made of a relatively high-index dielectric. They have a rectangular profile; the period of each sublayer is a, the width of dielectric strips is b, and the height is h. Upper and lower PCSs, separated by the gap g, are rotated in opposite directions each by $\alpha/2$. As a result, we deal with a moiré-periodic structure possessing second-order rotation symmetry for the x and y axes. In the scope of this paper, it is important that each of the sublayers supports photonic guided modes by itself. As a result of their interaction in specific moiré geometry, we obtain hybrid modes of unique optical properties.

The formation of a 2D-periodic moiré lattice makes the structure much more complicated for numerical consideration in contrast with its one-dimensional (1D)-periodic constituents. The small value of rotation angle α makes the unit cell of a superlattice correspondingly large and strongly increases the number of opened diffraction channels. As a result, both real-space-based numerical approaches such as the finite element method, finite difference time domain, and reciprocal-space-based Fourier modal method (FMM) [84,85]
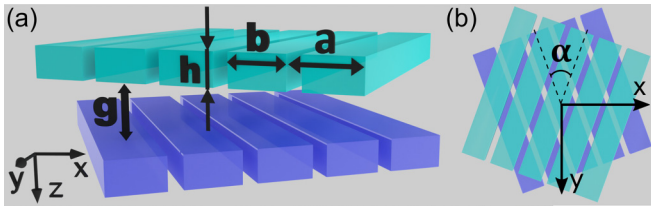
*Natalia.Salakhova@skoltech.ru

FIG. 1. The sketch of the moiré structure comprised twisted photonic crystal slabs: (a) general view and (b) top view.

become inefficient. For this reason, we apply our domestic-developed MA-FMM [54], which accounts for the peculiar structure of the considered 2D photonic crystal to obtain the scattering matrix of the twisted stack in a reasonable time.

To study the impact of the moiré pattern on the eigenmodes of the double-slab system, we calculate the in-plane wave vector dependence of the absorption coefficient of incident light. The results are obtained for the following structure parameters: The grating period is $a = 300$ nm, the dielectric strip width is $b = 250$ nm, the thickness of each slab is $h = 150$ nm, the gap size is $g = 300$ nm, and the rotation angle is $\alpha = 40°$. The dielectric constant of the gratings material is $\varepsilon = 6.25 + 0.01i$. We add a small imaginary part to the

dielectric permittivity to enable the absorption spectra that clearly indicate the excitation of resonant modes (see Fig. 2).

We start with the study of the isofrequency dispersion of the photonic modes. To excite them, we utilize the coupling prism with permittivity $\varepsilon_{prism} = 6.25$ that is placed at a distance $H = 300$ nm from the upper lattice. The absorption map for the s-polarized 1200-nm-wavelength light is shown in Fig. 2(a). The dispersion consists of two twisted ellipses, which correspond to the upper and lower sublayers. As a result of their interaction, we observe small areas of avoided crossing. In our scheme, the structure is excited by the strongly attenuating evanescent waves, so the excitation of the mode depends on the distance from the prism. Indeed, the brighter mode rotated in a clockwise direction relates to the upper lattice, whereas the darker mode rotated in the counterclockwise direction corresponds to the lower lattice.

If we consider the same spectrum for a slightly smaller 900-nm wavelength of light [see Fig. 2(b)], we immediately observe a rise of many additional branches of the guided modes. Indeed, they appear as a result of folding to the first Brillouin zone (FBZ) of the modes that expanded beyond its boundaries. It is worth noting that there are three pairs of FBZ boundaries. Two of them indicated by cyan and blue lines correspond to the diffraction on the upper
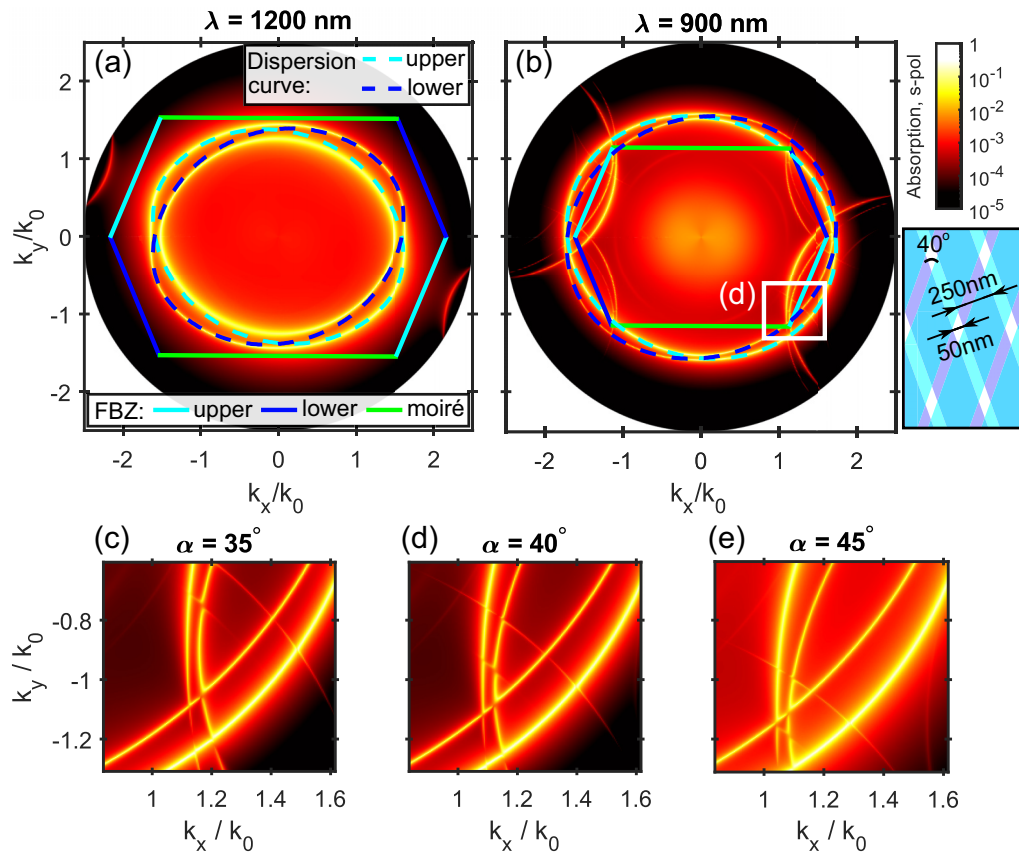

FIG. 2. Absorption maps of the stack of two identical one-dimensional (1D) photonic crystal slabs (PCSs) twisted by $\alpha = 40°$ for the s-polarized incident light with the wavelengths (a) $\lambda = 1200$ nm and (b) $\lambda = 900$ nm. The dashed cyan (blue) lines show the waveguide modes of the upper (lower) PCS in the absence of the lower (upper) one. Solid lines of cyan and blue colors in (a) and (b) denote boundaries of the first Brillouin zone (FBZ) corresponding to the periodicity of the upper and lower lattices. The green lines stand for the moiré-induced boundaries of the FBZ. (d) Enlarged version of the area indicated by the white box in (b). (c) and (e) Maps corresponding to the lattices of slightly different rotation angles $\alpha = 40° \pm 5°$.
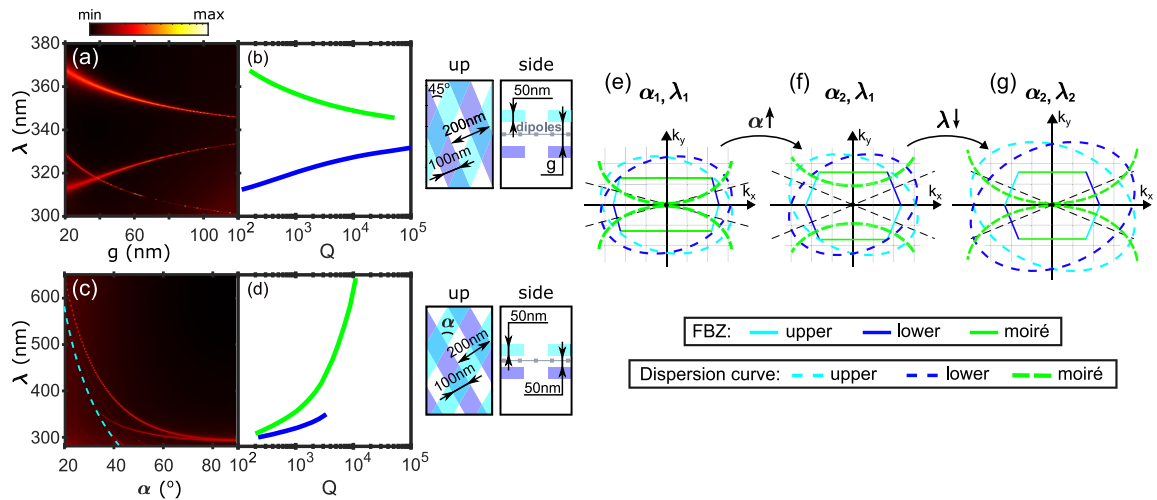
FIG. 3. The emission intensity of oscillating dipoles to the normal direction. The dipoles are uniformly distributed on the plane in the middle of the gap layer. Emission intensity is shown (a) as a function of the wavelength and the thickness of the gap layer and (c) as a function of the wavelength and the total rotation angle. In (c), the dashed cyan line denotes the opening of the lowest moiré-induced diffraction channel. (b) and (d) Quality factors Q of the corresponding modes from (a) and (c). Schematics of the considered structures are sketched next to (b) and (d). (e)–(g) Shift of a moiré mode under the change of the relative rotation angle and wavelength of light. Boundaries of the first Brillouin zone (FBZ) are denoted by solid lines, while the isofrequency contours of the modes are shown by dashed lines. The cyan (blue) lines correspond to the modes and boundaries of the FBZ corresponding to the upper (lower) sublattice, while the green lines correspond to the moiré-induced modes and boundaries.

and lower lattices, respectively, and are located at a distance π/a from the Γ point. The green pair corresponds to the moiré-induced diffraction along the y axis, which gives us $k_y = \pm \pi \sin(\alpha/2)/a$ boundaries in reciprocal space. Let us take a closer look at the region near the right bottom vertex of the FBZ [see Fig. 2(d) for an enlarged region from Fig. 2(b)]. Some of the modes are reflected from the cyan lamellar-grating-assisted boundaries, but the most narrow, barely noticeable modes originate as a reflection from the horizontal green boundary. In other words, they arise as a result of a coupling between the sublattices and therefore fully depend on their relative position and strength of the interaction. Even a slight change of the rotation angle α results in a shift of the green boundaries of the FBZ [$k_y = \pm \pi \sin(\alpha/2)/a$] and corresponding moiré modes. The absorption maps for three close angles $\alpha = 35°$, $40°$, and $45°$ [see Figs. 2(c)–2(e)] demonstrate that $5°$ deviation almost does not affect the wide modes of upper and lower sublattices but strongly shifts the narrow lines of hybrid resonances.

So far, we used the coupling prism for the excitation of the system eigenmodes from the far field. Although such an approach is a rather simple way of plotting dispersion curves, it cannot be implemented for the characterization of the quality factor of the modes. Indeed, the exciting prism automatically enables the leakage of the modes. Moreover, some of the losses come from the material absorption in the slabs, which we introduced previously. Therefore, to study the quality factor of the moiré modes, from now on, we use a nondissipative slab ($\varepsilon = 6.25 + 0i$; see Appendix B to find the effect of dissipation on the quality factor) and excite the eigenmodes by uniformly distributed dipoles oscillating within the xy plane; dipoles are placed in the middle of the gap layer, and their emission is not correlated (we sum the intensities of separate dipoles radiation but not their fields). Geometric

parameters of the structure are chosen in such a way that the isofrequency contours of the moiré-induced modes pass through the Γ point [see sketch in Fig. 3(g) for the values of $a = 200$ nm, $b = 100$ nm, and $h = 50$ nm]. To study the hybrid modes, we calculate spectra of far-field emission intensity in the normal direction (see Appendix A for details on the calculation of dipole emission using the FMM). Our primary interest is concentrated on the dependence of the modes on the relative position of the sublattices, which is characterized by the gap size g and angle α.

The calculated gap-size dependence of the emissivity spectrum is shown in Fig. 3(a) for the rotation angle $\alpha = 45°$. The smaller the gap size, the stronger the near-field interaction between the eigenmodes of the sublattices, and hence, the larger the spectral distance between the hybridized moiré modes. When the gap size between two sublattices is relatively large, the interaction between them weakens, and lines of hybrid modes approach each other. Moreover, their quality factor rapidly increases and tends to infinity [see Fig. 3(b)]. Indeed, the existence of the hybrid mode at the Γ point is determined by the coupling between the upper and lower sublattices, which is ensured by the evanescent, exponentially decaying harmonics. For a large distance between the constituents of the stack, coupling strength becomes a small parameter, whose nonzero value determines the finite width of the mode. Therefore, the variation of the gap size might be used to control the spectral position and the quality factor of the moiré-induced modes in a wide range. In the considered case, the gap size in the range of 20–120 nm provides the spectral shift of hybrid modes by up to ≈ 20 nm and simultaneously changes their quality factor within the range from 10^2 to 10^5 [see Figs. 3(a) and 3(b)].

Let us now study how the rotation of the PCSs affects the hybrid modes. For this purpose, we calculate the depen-
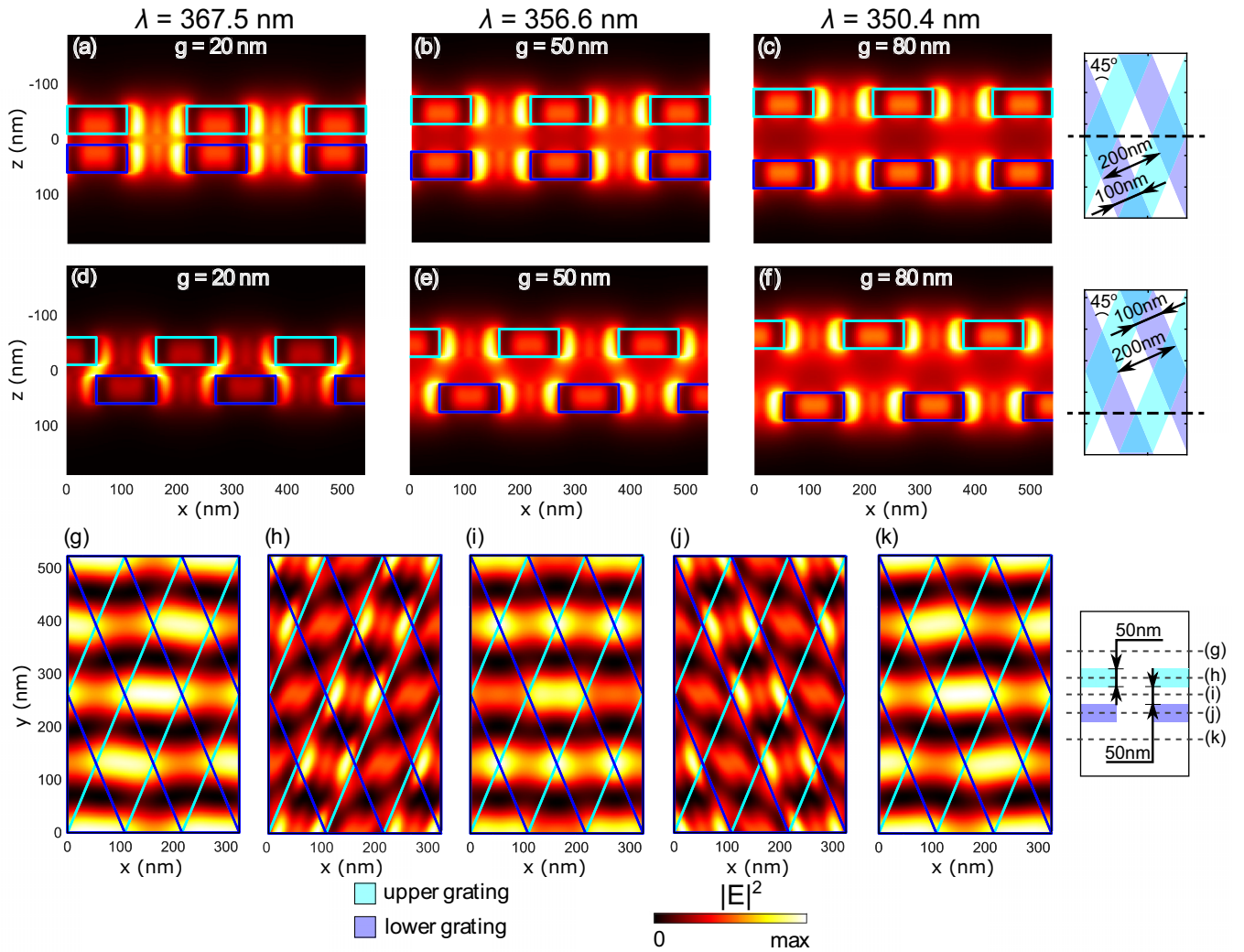
FIG. 4. The eigenmode electric field intensity in different sections for a structure with parameters $a = 200$ nm, $b = 100$ nm, $h = 50$ nm, and $\alpha = 45°$. (a), (b), (c) and (d), (e), (f) show the field distribution in the x-z (vertical) plane for three different thicknesses of the gap layer $g = 20$, 50, and 80 nm and for two different cross-sections indicated in the right column. (g)–(k) Electric field distribution in five x-y (horizontal) planes. The uppermost (g) and lowermost (k) horizontal cross-sections are taken at 50 nm distance from the nearest interface, while the rest of the horizontal cross-sections (h)–(j) lay in the middle of the layers. The dielectric stripes of the upper (lower) layer are denoted by cyan (blue) color.

dence of the emissivity spectra on the relative rotation angle α [Fig. 3(c)]. The cyan dashed line shows the first of the so-called Rayleigh anomalies, which in our case indicates the opening of the moiré-induced diffraction channel. Both hybrid modes of the structure are observed above the cyan line, where the diffraction is closed and leakage losses are suppressed. For the case of perpendicular sublattices ($\alpha = 90°$), there are two mirror symmetry planes, which makes the modes degenerate. The spectral position and width of each resonance are very sensitive to the α angle [see Figs. 3(c) and 3(d)]. In the presented structure with the gap size $g = 50$ nm, by changing the relative rotation angle from $\alpha = 90°$ to $\alpha = 20°$, we can tune the wavelength of the moiré-induced modes in a wide range from 300 to 650 nm [see Fig. 3(c)], and together with a redshift of the resonant wavelength, the Q factor can be boosted from $\approx 10^2$ to 10^4 [see Fig. 3(d)].

To clarify the reason for such a rapid wavelength shift of the resonances, we consider the modification of the FBZ

and optical mode dispersion with a change of the rotation angle. Figure 3(e) schematically shows the dispersion of the moiré-induced modes (green dashed lines) that pass through the Γ point. A slight increase of α results in growth of the moiré Bragg vector $G_{\mathrm{moire}} = |\vec{G}_{\mathrm{upper}} - \vec{G}_{\mathrm{lower}}| = \frac{4\pi}{a} \sin \frac{\alpha}{2}$, deformation of the FBZ, and split of the modes [see Fig. 3(f)]. To bring them back to the Γ point, we need to reduce the considered wavelength and increase the radius of the corresponding modes [see Fig. 3(g)]. Since the position of the FBZ boundary is rather sensitive to the angle, the energy of the modes becomes sensitive as well. Importantly, together with a movement of resonant modes, corresponding Fourier harmonics shift in reciprocal space. If the harmonics ensuring coupling of the modes possess relatively large in-plane components $\vec{k}_{\parallel}$ of the wave vector, they rapidly decay along the z axis [$\propto \exp(-\mathrm{Im}\sqrt{k^2 - k_{\parallel}^2}z)$]. Consequently, the only channel of leakage through the scattering on the neighboring

lattice is suppressed, and quality factors of corresponding hybrid modes are rather high.

Finally, we theoretically study the near field of the long-wavelength (low-energy) mode from Fig. 3. Figures 4(a)–4(c) demonstrate the distribution of the electric field $|\mathbf{E}|^2$ of the hybrid modes in stacks of different gap sizes for the vertical section ($y = $ const.) in which dielectric strips lie directly over the other strips. Figures 4(d)–4(f) consider the same modes for the vertical section in which strips of upper and lower sublattices alternate with each other. In both cases, the field is localized near the dielectric slabs with a notable enhancement in the vicinity of the edges of the dielectric strips. For a small value of the gap size ($g = 20$ nm), we observe a significant concentration of the field between the sublattices, especially in Fig. 4(d), which indicates strong coupling between their modes. Nevertheless, with a slight increase in the thickness, we immediately see that the field near each of the structures is determined primarily by its own eigenmodes, whereas the hybridization is responsible for their relative phases. The symmetric intensity maps in Figs. 4(a)–4(c) might give a misleading impression that the considered moiré modes possess corresponding symmetry as well, but Figs. 4(d)–4(f) clearly show that the modes evolve along the strips, and none of the sections by themselves can provide us with the full picture.

The distribution of the electric field intensity of the eigenmode in five horizontal sections is illustrated in Figs. 4(g)–4(k). We consider the field in the middle of all three layers [see panels (h)–(j)] and at a 50-nm distance from them [see panels (g) and (k)]. The most important feature of the field is the standing wave clearly observed in panels (i) and (g), (k). This pattern is associated with guided modes of both sublattices propagating in opposite directions of the y axis. The field of standing waves in each specific section is slightly affected by the adjacent dielectric strips, which is clearly seen in Figs. 4(g), 4(i) and 4(k). Interestingly, the larger the distance from the section to the lattice, the clearer the picture of the standing waves should be due to the extinction of high-$k_\parallel$ Fourier harmonics. For the sections of upper and lower sublattices [see Figs. 4(h) and 4(j)], we observe rather complicated field distribution with plenty of peculiarities such as hot spots localized near the dielectric-vacuum interfaces.

III. CONCLUSIONS

In conclusion, we studied twisted stacks of identical PCSs and demonstrated an emergence of specific moiré modes due to interlayer interaction. These modes are very sensitive to the angle of relative rotation of the sublayers α and the gap size between them g. We managed to tune the mode wavelength in the range of 300–600 nm and vary the quality factor from 10^2 up to 10^5 for a nondissipative demonstration structure. The demonstrated results show the moiré structure potential for engineering high-quality optical resonances, their active tuning, and their application in optomechanical devices and chiral nanophotonics.
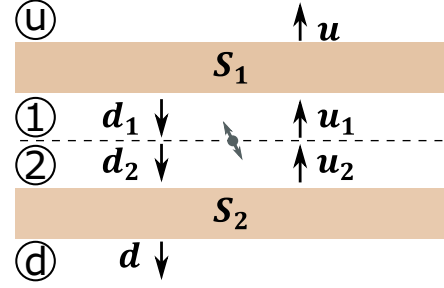
ACKNOWLEDGMENT

FIG. 5. Schematic view of the structure for calculation of the oscillation dipole emission. Two rectangles correspond to the upper and lower lattices with scattering matrices S_1 and S_2, respectively. The vectors $d_{1(2)}$ and $u_{1(2)}$ are the vectors of amplitudes propagating in opposite directions between the two lattices. The vectors u and d are the vectors of amplitudes of the fields outside the system.

APPENDIX A: CALCULATION OF DIPOLE EMISSION

The power flow of the emission from an oscillating point dipole in the up and down directions perpendicular to the structure can be calculated as a z projection of the Poynting vector sum up over the Floquet-Fourier harmonics:

$$P = \frac{c}{16\pi}(E_x^\dagger H_y + E_x H_y^\dagger - E_y^\dagger H_x - E_y H_x^\dagger), \qquad \text{(A1)}$$

where $E_{x,y}$ and H_x, y are the hypervectors of Floquet-Fourier components of electric and magnetic fields, $E_{x,y}^\dagger$ and $H_{x,y}^\dagger$ are the conjugated transpose hypervectors, and c is the speed of light.

The calculation of the field components can be provided using the scattering matrix approach [86–88]. We use the FMM in scattering matrix form [84], where the field components $\vec{E} = \begin{bmatrix} E_x \\ E_y \end{bmatrix}$ and

$\vec{H} = \begin{bmatrix} H_x \\ H_y \end{bmatrix}$ in each area are defined by the material matrix $\mathbb{F}$ from the vectors of field amplitudes $\vec{u}$, $\vec{d}$:

$$\begin{bmatrix} \vec{E} \\ \vec{H} \end{bmatrix}_u = \mathbb{F}_u \begin{bmatrix} \vec{0} \\ \vec{u} \end{bmatrix}, \qquad \begin{bmatrix} \vec{E} \\ \vec{H} \end{bmatrix}_d = \mathbb{F}_d \begin{bmatrix} \vec{d} \\ \vec{0} \end{bmatrix}, \qquad \text{(A2)}$$

$$\begin{bmatrix} \vec{E}_1 \\ \vec{H}_1 \end{bmatrix} = \mathbb{F} \begin{bmatrix} \vec{d}_1 \\ \vec{u}_1 \end{bmatrix}, \qquad \begin{bmatrix} \vec{E}_2 \\ \vec{H}_2 \end{bmatrix} = \mathbb{F} \begin{bmatrix} \vec{d}_2 \\ \vec{u}_2 \end{bmatrix}. \qquad \text{(A3)}$$

The vectors of amplitudes are shown in Fig. 5, and indices u, d, 1, and 2 indicate where these corresponding quantities are taken. We have also utilized the fact that $\mathbb{F}_1 = \mathbb{F}_2 = \mathbb{F}$. The vector $\vec{0}$ is a zero vector of the same size as $\vec{u}$ and $\vec{d}$, which indicates the fact that, in the emission problem, there is no incoming wave.

Moreover, from scattering matrix formalism, the vectors of amplitudes in different areas are connected:

$$\begin{bmatrix} \vec{d}_1 \\ \vec{u} \end{bmatrix} = \begin{bmatrix} S_1^{dd} & S_1^{du} \\ S_1^{ud} & S_1^{uu} \end{bmatrix} \begin{bmatrix} \vec{0} \\ \vec{u}_1 \end{bmatrix}, \qquad \begin{bmatrix} \vec{d} \\ \vec{u}_2 \end{bmatrix} = \begin{bmatrix} S_2^{dd} & S_2^{du} \\ S_2^{ud} & S_2^{uu} \end{bmatrix} \begin{bmatrix} \vec{d}_2 \\ \vec{0} \end{bmatrix}.$$
$$\text{(A4)}$$

The oscillating dipole source with space coordinate $\vec{r}_0$ is simulated as a current $\vec{J}$ with Floquet-Fourier components:

$$J_{x,y,z} = j_{x,y,z} \exp[-i\vec{r}_0(\vec{k}_\parallel + \vec{G}_{nm})], \qquad \text{(A5)}$$

where $\vec{G}_{nm} = [2\pi n/a, 2\pi m/a]$ is a Bragg vector, and n and m are integers indicating the harmonic. The $j_{x,y,z}$ are the components of the current in real space, and $\vec{j} = [1, \pm i, 0]$, where the sign $-$ or $+$ corresponds to the clockwise or counterclockwise rotating dipole. To simulate a linearly polarized dipole, we use currents with both signs simultaneously.

According to the Maxwell equation:

$$\nabla \times \mathbf{H} = \frac{4\pi}{c}\mathbf{J} - i\hat{\varepsilon}\frac{\omega}{c}\mathbf{E},$$

the electric and magnetic fields are discontinuous at the plane of dipole positioning [86], which results in additional internal boundary condition on the in-plane components [87]:

$$\begin{bmatrix} \vec{E}_2 \\ \vec{H}_2 \end{bmatrix} - \begin{bmatrix} \vec{E}_1 \\ \vec{H}_1 \end{bmatrix} = \begin{bmatrix} \vec{J}_E \\ \vec{J}_H \end{bmatrix}. \quad (A6)$$

In the case when the tensor of dielectric permittivity is diagonal,

$$\vec{J}_E = \frac{4\pi}{\omega}\begin{bmatrix} K_x \\ K_y \end{bmatrix}\hat{\varepsilon}_{33}^{-1}J_z, \quad \vec{J}_H = \frac{4\pi}{c}\begin{bmatrix} J_y \\ -J_x \end{bmatrix}. \quad (A7)$$

Here, $K_{x,y}$ is a diagonal matrix with values of the in-plane component of the wave vector for different diffraction orders, and $\hat{\varepsilon}_{33}^{-1}$ is a matrix obtained from the Fourier transform of the dielectric permittivity.

From Eqs. (A3) and (A6), we get

$$\begin{bmatrix} \vec{d}_2 \\ \vec{u}_2 \end{bmatrix} - \begin{bmatrix} \vec{d}_1 \\ \vec{u}_1 \end{bmatrix} = \mathbb{F}^{-1}\begin{bmatrix} \vec{J}_E \\ \vec{J}_H \end{bmatrix} = \begin{bmatrix} \vec{J}_d \\ \vec{J}_u \end{bmatrix}. \quad (A8)$$

According to Eq. (A4),

$$\vec{u} = S_1^{uu}\vec{u}_1, \quad \vec{d} = S_2^{dd}\vec{d}_2. \quad (A9)$$

To find $\vec{u}$ and $\vec{d}$, we express the vectors $\vec{u}_1$ and $\vec{d}_2$ from Eq. (A8), substituting $\vec{d}_1 = S_1^{du}\vec{u}_1$ and $\vec{u}_2 = S_2^{ud}\vec{d}_2$:

$$\vec{d}_2 = \left(\mathbb{I} - S_1^{du}S_2^{ud}\right)^{-1}\left(\vec{J}_d - S_1^{du}\vec{J}_u\right),$$
$$\vec{u}_1 = \left(S_2^{ud}S_1^{du} - \mathbb{I}\right)^{-1}\left(\vec{J}_u - S_2^{ud}\vec{J}_d\right), \quad (A10)$$

Finally, we obtain the expressions for the external vector of amplitudes:

$$\vec{d} = S_2^{dd}\left(\mathbb{I} - S_1^{du}S_2^{ud}\right)^{-1}\left(\vec{J}_d - S_1^{du}\vec{J}_u\right),$$
$$\vec{u} = S_1^{uu}\left(S_2^{ud}S_1^{du} - \mathbb{I}\right)^{-1}\left(\vec{J}_u - S_2^{ud}\vec{J}_d\right). \quad (A11)$$
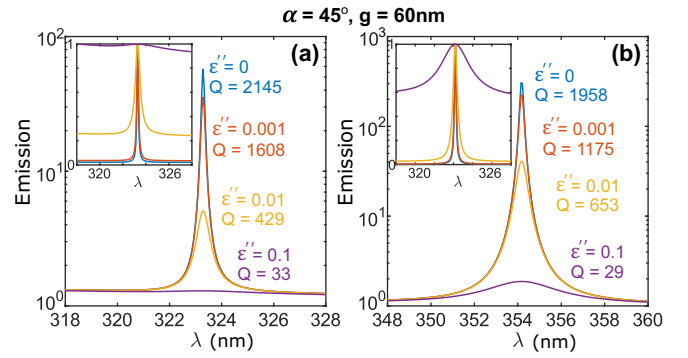

FIG. 6. Spectra of the emission intensity to the normal. (a) Short-wavelength and (b) long-wavelength resonant modes from Fig. 3. The blue lines show emission of lossless structure. The orange, yellow, and purple lines show results for lossy materials with three different values of the imaginary part of the dielectric permittivity $\varepsilon'' = 0.001, 0.01,$ and 0.1 relatively. The insets show the same spectra normalized to the maximum.

Substitution of $\vec{u}$ and $\vec{d}$ into Eq. (A2) provides the required components of electric and magnetic fields and allows us to calculate the emission of the dipole source.

APPENDIX B: DISSIPATIVE LOSS EFFECT ON THE MOIRÉ MODE QUALITY FACTOR

In the main text, we focused on the radiative losses of the modes as a function of the geometrical parameters. To study how dissipative losses affect the quality factor, we calculate the spectra of emission intensity for structures with different dissipative materials of the PCSs.

In Fig. 6, the presence of a nonzero imaginary part of the dielectric permittivity decreases the emissivity of the dipoles from the structure and impairs the quality of the modes. However, no shift of the resonant wavelength of the modes is observed for both (a) short-wavelength and (b) long-wavelength modes from Figs. 3(a) and 3(c). Dissipative losses are not sensitive to some geometrical parameter changes since they mainly depend on the field confinement in dissipative material. Thus, the position of the resonant peak is defined by radiative losses when dissipative losses decrease peak intensity with increasing dissipation which, in turn, leads to correspondingly low Q factors.

[1] Y. Chang, D. Hasan, B. Dong, J. Wei, Y. Ma, G. Zhou, K. W. Ang, and C. Lee, All-dielectric surface-enhanced infrared absorption-based gas sensor using guided resonance, ACS Appl. Mater. Interfaces **10**, 38272 (2018).

[2] Y. Wang, D. Zhu, Z. Cui, L. Yue, X. Zhang, L. Hou, K. Zhang, and H. Hu, Properties and sensing performance of all-dielectric metasurface THz absorbers, IEEE Trans. Terahertz Sci. Technol. **10**, 599 (2020).

[3] K. Lodewijks, W. Van Roy, G. Borghs, L. Lagae, and P. Van Dorpe, Boosting the figure-of-merit of LSPR-based refractive index sensing by phase-sensitive measurements, Nano Lett. **12**, 1655 (2012).

[4] S. R. K. Rodriguez, A. Abass, B. Maes, O. T. A. Janssen, G. Vecchi, and J. Gómez Rivas, Coupling Bright and Dark Plasmonic Lattice Resonances, Phys. Rev. X **1**, 021019 (2011).

[5] Y. Shen, J. Zhou, T. Liu, Y. Tao, R. Jiang, M. Liu, G. Xiao, J. Zhu, Z.-K. Zhou, X. Wang *et al.*, Plasmonic gold mushroom arrays with refractive index sensing figures of merit approaching the theoretical limit, Nat. Commun. **4**, 2381 (2013).

[6] S. Yuan, X. Qiu, C. Cui, L. Zhu, Y. Wang, Y. Li, J. Song, Q. Huang, and J. Xia, Strong photoluminescence enhancement in all-dielectric Fano metasurface with high quality factor, ACS Nano **11**, 10704 (2017).

[7] A. Krasnok, S. Glybovski, M. Petrov, S. Makarov, R. Savelev, P. Belov, C. Simovski, and Y. Kivshar, Demonstration of the enhanced Purcell factor in all-dielectric structures, Appl. Phys. Lett. **108**, 211105 (2016).

[8] Y. Yang, V. A. Zenin, and S. I. Bozhevolnyi, Anapole-assisted strong field enhancement in individual all-dielectric nanostructures, ACS Photonics **5**, 1960 (2018).

[9] Z. Liu, Y. Xu, Y. Lin, J. Xiang, T. Feng, Q. Cao, J. Li, S. Lan, and J. Liu, High-Q Quasibound States in the Continuum for Nonlinear Metasurfaces, Phys. Rev. Lett. **123**, 253901 (2019).

[10] D. Smirnova and Y. S. Kivshar, Multipolar nonlinear nanophotonics, Optica **3**, 1241 (2016).

[11] M. R. Shcherbakov, D. N. Neshev, B. Hopkins, A. S. Shorokhov, I. Staude, E. V. Melik-Gaykazyan, M. Decker, A. A. Ezhov, A. E. Miroshnichenko, I. Brener *et al.*, Enhanced third-harmonic generation in silicon nanoparticles driven by magnetic response, Nano Lett. **14**, 6488 (2014).

[12] L. Wang, S. Kruk, K. Koshelev, I. Kravchenko, B. Luther-Davies, and Y. Kivshar, Nonlinear wavefront control with all-dielectric metasurfaces, Nano Lett. **18**, 3978 (2018).

[13] S. Noda, K. Kitamura, T. Okino, D. Yasuda, and Y. Tanaka, Photonic-crystal surface-emitting lasers: Review and introduction of modulated-photonic crystals, IEEE J. Sel. Top. Quantum Electron. **23**, 1 (2017).

[14] D. Wang, A. Yang, W. Wang, Y. Hua, R. D. Schaller, G. C. Schatz, and T. W. Odom, Band-edge engineering for controlled multi-modal nanolasing in plasmonic superlattices, Nat. Nanotechnol. **12**, 889 (2017).

[15] P. Melentiev, A. Kalmykov, A. Gritchenko, A. Afanasiev, V. Balykin, A. Baburin, E. Ryzhova, I. Filippov, I. Rodionov, I. Nechepurenko *et al.*, Plasmonic nanolaser for intracavity spectroscopy and sensorics, Appl. Phys. Lett. **111**, 213104 (2017).

[16] A. A. Zyablovsky, I. A. Nechepurenko, E. S. Andrianov, A. V. Dorofeenko, A. A. Pukhov, A. P. Vinogradov, and A. A. Lisyansky, Optimum gain for plasmonic distributed feedback lasers, Phys. Rev. B **95**, 205417 (2017).

[17] I. M. Fradkin, S. A. Dyakov, and N. A. Gippius, Nanoparticle lattices with bases: Fourier modal method and dipole approximation, Phys. Rev. B **102**, 045432 (2020).

[18] I. M. Fradkin, A. A. Demenev, V. D. Kulakovskii, V. N. Antonov, and N. A. Gippius, Plasmonic grating for circularly polarized outcoupling of waveguide-enhanced spontaneous emission, Appl. Phys. Lett. **120**, 171702 (2022).

[19] G. Zheng, H. Mühlenbernd, M. Kenney, G. Li, T. Zentgraf, and S. Zhang, Metasurface holograms reaching 80% efficiency, Nat. Nanotechnol. **10**, 308 (2015).

[20] W. Ye, F. Zeuner, X. Li, B. Reineke, S. He, C.-W. Qiu, J. Liu, Y. Wang, S. Zhang, and T. Zentgraf, Spin and wavelength multiplexed nonlinear metasurface holography, Nat. Commun. **7**, 11930 (2016).

[21] Q. Wei, L. Huang, X. Li, J. Liu, and Y. Wang, Broadband multiplane holography based on plasmonic metasurface, Adv. Opt. Mater. **5**, 1700434 (2017).

[22] A. Ignatov and A. Merzlikin, Excitation of plasmonic waves in metal–dielectric structures by a laser beam using holography principles, Opt. Commun. **410**, 83 (2018).

[23] N. Yu and F. Capasso, Flat optics with designer metasurfaces, Nat. Mater. **13**, 139 (2014).

[24] H.-T. Chen, A. J. Taylor, and N. Yu, A review of metasurfaces: Physics and applications, Rep. Prog. Phys. **79**, 076401 (2016).

[25] A. V. Kildishev, A. Boltasseva, and V. M. Shalaev, Planar photonics with metasurfaces, Science **339**, 1232009 (2013).

[26] S. Baur, S. Sanders, and A. Manjavacas, Hybridization of lattice resonances, ACS Nano **12**, 1618 (2018).

[27] R. Kolkowski and A. F. Koenderink, Lattice resonances in optical metasurfaces with gain and loss, Proc. IEEE **108**, 795 (2019).

[28] A. D. Humphrey and W. L. Barnes, Plasmonic surface lattice resonances on arrays of different lattice symmetry, Phys. Rev. B **90**, 075404 (2014).

[29] L. Zundel, A. May, and A. Manjavacas, Lattice resonances induced by periodic vacancies in arrays of nanoparticles, ACS Photonics **8**, 360 (2021).

[30] S. Linden, A. Christ, J. Kuhl, and H. Giessen, Selective suppression of extinction within the plasmon resonance of gold nanoparticles, Appl. Phys. B: Lasers Opt. **73**, 311 (2001).

[31] I. M. Fradkin, S. A. Dyakov, and N. A. Gippius, Thickness-Independent Narrow Resonance in a Stack of Plasmonic Lattices, Phys. Rev. Appl. **14**, 054030 (2020).

[32] K. Voronin, A. S. Taradin, M. V. Gorkunov, and D. G. Baranov, Single-handedness chiral optical cavities, ACS Photonics **9**, 2652 (2022).

[33] D. Becerril, G. Pirruccio, and C. Noguez, Optical band engineering via vertical stacking of honeycomb plasmonic lattices, Phys. Rev. B **103**, 195412 (2021).

[34] S. Murai, K. Agata, and K. Tanaka, Photoluminescence from an emitter layer sandwiched between the stack of metasurfaces, J. Appl. Phys. **129**, 183101 (2021).

[35] X.-D. Chen, X.-T. He, and J.-W. Dong, All-dielectric layered photonic topological insulators, Laser Photonics Rev. **13**, 1900091 (2019).

[36] S. Chen, Y. Zhang, Z. Li, H. Cheng, and J. Tian, Empowered layer effects and prominent properties in few-layer metasurfaces, Adv. Opt. Mater. **7**, 1801477 (2019).

[37] A. Berkhout and A. F. Koenderink, Perfect absorption and phase singularities in plasmon antenna array etalons, ACS Photonics **6**, 2917 (2019).

[38] L. Balents, C. R. Dean, D. K. Efetov, and A. F. Young, Superconductivity and strong correlations in moiré flat bands, Nat. Phys. **16**, 725 (2020).

[39] G. Chen, A. L. Sharpe, P. Gallagher, I. T. Rosen, E. J. Fox, L. Jiang, B. Lyu, H. Li, K. Watanabe, T. Taniguchi *et al.*, Signatures of tunable superconductivity in a trilayer graphene moiré superlattice, Nature (London) **572**, 215 (2019).

[40] Y. Cao, V. Fatemi, S. Fang, K. Watanabe, T. Taniguchi, E. Kaxiras, and P. Jarillo-Herrero, Unconventional superconductivity in magic-angle graphene superlattices, Nature (London) **556**, 43 (2018).

[41] J. H. Pixley and E. Y. Andrei, Ferromagnetism in magic-angle graphene, Science **365**, 543 (2019).

[42] A. L. Sharpe, E. J. Fox, A. W. Barnard, J. Finney, K. Watanabe, T. Taniguchi, M. A. Kastner, and D. Goldhaber-Gordon, Emergent ferromagnetism near three-quarters filling in twisted bilayer graphene, Science **365**, 605 (2019).

[43] G. Chen, A. L. Sharpe, E. J. Fox, Y. H. Zhang, S. Wang, L. Jiang, B. Lyu, H. Li, K. Watanabe, T. Taniguchi *et al.*, Tunable correlated Chern insulator and ferromagnetism in a moiré superlattice, Nature (London) **579**, 56 (2020).

[44] C. Repellin, Z. Dong, Y. H. Zhang, and T. Senthil, Ferromagnetism in Narrow Bands of Moiré Superlattices, Phys. Rev. Lett. **124**, 187601 (2020).

[45] G. Li, A. Luican, J. M. Lopes Dos Santos, A. H. Castro Neto, A. Reina, J. Kong, and E. Y. Andrei, Observation of Van Hove singularities in twisted graphene layers, Nat. Phys. **6**, 109 (2010).

[46] Y. Jiang, X. Lai, K. Watanabe, T. Taniguchi, K. Haule, J. Mao, and E. Y. Andrei, Charge order and broken rotational symmetry in magic-angle twisted bilayer graphene, Nature (London) **573**, 91 (2019).

[47] K. Slagle and L. Fu, Charge transfer excitations, pair density waves, and superconductivity in moiré materials, Phys. Rev. B **102**, 235423 (2020).

[48] E. Y. Andrei, D. K. Efetov, P. Jarillo-Herrero, A. H. MacDonald, K. F. Mak, T. Senthil, E. Tutuc, A. Yazdani, and A. F. Young, The marvels of moiré materials, Nat. Rev. Mater. **6**, 201 (2021).

[49] W. Ma, F. Cheng, and Y. Liu, Deep-learning-enabled on-demand design of chiral metamaterials, ACS Nano **12**, 6326 (2018).

[50] H. X. Xu, G. Hu, L. Han, M. Jiang, Y. Huang, Y. Li, X. Yang, X. Ling, L. Chen, J. Zhao *et al.*, Chirality-assisted high-efficiency metasurfaces with independent control of phase, amplitude, and polarization, Adv. Opt. Mater. **7**, 1801479 (2019).

[51] Y. Zhao, A. N. Askarpour, L. Sun, J. Shi, X. Li, and A. Alù, Chirality detection of enantiomers using twisted optical metamaterials, Nat. Commun. **8**, 14180 (2017).

[52] G. Hu, M. Wang, Y. Mazor, C. W. Qiu, and A. Alù, Tailoring light with layered and moiré metasurfaces, Trends Chem. **3**, 342 (2021).

[53] O. Aftenieva, M. Schnepf, B. Mehlhorn, and T. A. König, Tunable circular dichroism by photoluminescent moiré gratings, Adv. Opt. Mater. **9**, 2001280 (2021).

[54] N. S. Salakhova, I. M. Fradkin, S. A. Dyakov, and N. A. Gippius, Fourier modal method for moiré lattices, Phys. Rev. B **104**, 085424 (2021).

[55] M. K. Chen, J. C. Zhang, C. W. Leung, L. Sun, Y. Fan, Y. Liang, J. Yao, X. Liu, J. Yuan, Y. Xu *et al.*, Chiral-magic angle of nanoimprint meta-device, Nanophotonics (2023), doi:10.1515/nanoph-2022-0733.

[56] G. Hu, A. Krasnok, Y. Mazor, C. W. Qiu, and A. Alù, Moiré hyperbolic metasurfaces, Nano Lett. **20**, 3217 (2020).

[57] G. Hu, Q. Ou, G. Si, Y. Wu, J. Wu, Z. Dai, A. Krasnok, Y. Mazor, Q. Zhang, Q. Bao *et al.*, Topological polaritons and photonic magic angles in twisted α-MoO$_3$ bilayers, Nature (London) **582**, 209 (2020).

[58] M. Chen, X. Lin, T. H. Dinh, Z. Zheng, J. Shen, Q. Ma, H. Chen, P. Jarillo-Herrero, and S. Dai, Configurable phonon polaritons in twisted α-MoO$_3$, Nat. Mater. **19**, 1307 (2020).

[59] J. Duan, N. Capote-Robayna, J. Taboada-Gutiérrez, G. Álvarez-Pérez, I. Prieto, J. Martín-Sánchez, A. Y. Nikitin, and P. Alonso-González, Twisted nano-optics: Manipulating light at the nanoscale with twisted phonon polaritonic slabs, Nano Lett. **20**, 5323 (2020).

[60] Z. Zheng, F. Sun, W. Huang, J. Jiang, R. Zhan, Y. Ke, H. Chen, and S. Deng, Phonon polaritons in twisted double-layers of hyperbolic van der Waals crystals, Nano Lett. **20**, 5301 (2020).

[61] O. G. Matveeva, A. I. F. Tresguerres-Mata, R. V. Kirtaev, K. V. Voronin, J. Taboada-Gutiérrez, C. Lanza-García, J. Duan, J. Martín-Sánchez, V. S. Volkov, P. Alonso-González *et al.*, Twist-

tunable polaritonic nanoresonators in a van der Waals crystal, arXiv:2206.14886.

[62] K. Y. Lee, K. W. Yoo, S. Cheon, W.-J. Joo, J. W. Yoon, and S. H. Song, Synthetic Topological Nodal Phase in Bilayer Resonant Gratings, Phys. Rev. Lett. **128**, 053002 (2022).

[63] J. Zeng, Y. Hu, X. Zhang, S. Fu, H. Yin, Z. Li, and Z. Chen, Localization-to-delocalization transition of light in frequency-tuned photonic moiré lattices, Opt. Express **29**, 25388 (2021).

[64] M. Martí-Sabaté and D. Torrent, Dipolar Localization of Waves in Twisted Phononic Crystal Plates, Phys. Rev. Appl. **15**, L011001 (2020).

[65] P. Wang, Y. Zheng, X. Chen, C. Huang, Y. V. Kartashov, L. Torner, V. V. Konotop, and F. Ye, Localization and delocalization of light in photonic moiré lattices, Nature (London) **577**, 42 (2020).

[66] H. Tang, X. Ni, F. Du, V. Srikrishna, and E. Mazur, On-chip light trapping in bilayer moiré photonic crystal slabs, Appl. Phys. Lett. **121**, 231702 (2022).

[67] A. A. Arkhipova, Y. V. Kartashov, S. K. Ivanov, S. A. Zhuravitskii, N. N. Skryabin, I. V. Dyakonov, A. A. Kalinkin, S. P. Kulik, V. O. Kompanets, S. V. Chekalin *et al.*, Observation of Linear and Nonlinear Light Localization at the Edges of Moiré Arrays, Phys. Rev. Lett. **130**, 083801 (2023).

[68] H. Yang, J. Zhai, S. Huo, Z. Wang, D. Chen, and X. Sun, Localization of light in 2D photonic moiré superlattices, J. Phys. D **55**, 495111 (2022).

[69] D. X. Nguyen, X. Letartre, E. Drouard, P. Viktorovitch, H. C. Nguyen, and H. S. Nguyen, Magic configurations in moiré superlattice of bilayer photonic crystals: Almost-perfect flatbands and unconventional localization, Phys. Rev. Res. **4**, L032031 (2022).

[70] B. Lou and S. Fan, Tunable frequency filter based on twisted bilayer photonic crystal slabs, ACS Photonics **9**, 800 (2022).

[71] B. Lou, B. Wang, J. A. Rodríguez, M. Cappelli, and S. Fan, Tunable guided resonance in twisted bilayer photonic crystal, Sci. Adv. **8**, eadd4339 (2022).

[72] S. Liu, S. Ma, R. Shao, L. Zhang, T. Yan, Q. Ma, S. Zhang, and T. J. Cui, Moiré metasurfaces for dynamic beamforming, Sci. Adv. **8**, eabo1511 (2022).

[73] C.-L. Zhou, Y. Zhang, and H.-L. Yi, Moiré-driven reconstitution on electromagnetic energy transfer, Mater. Today Phys. **28**, 100891 (2022).

[74] H. Tang, F. Du, S. Carr, C. DeVault, O. Mello, and E. Mazur, Modeling the optical properties of twisted bilayer photonic crystals, Light Sci. Appl. **10**, 157 (2021).

[75] P. Hong, L. Xu, C. Ying, and M. Rahmani, Flatband mode in photonic moiré superlattice for boosting second-harmonic generation with monolayer van der Waals crystals, Opt. Lett. **47**, 2326 (2022).

[76] C.-H. Yi, H. C. Park, and M. J. Park, Strong interlayer coupling and stable topological flat bands in twisted bilayer photonic moiré superlattices, Light Sci. Appl. **11**, 289 (2022).

[77] K. Alnasser, S. Kamau, N. Hurley, J. Cui, and Y. Lin, Photonic band gaps and resonance modes in 2D twisted moiré photonic crystal, Photonics **8**, 408 (2021).

[78] X. Letartre, S. Mazauric, S. Cueff, T. Benyattou, H. S. Nguyen, and P. Viktorovitch, Analytical non-hermitian description of photonic crystals with arbitrary lateral and transverse symmetry, Phys. Rev. A **106**, 033510 (2022).

[79] B. Gai and J. Guo, Collective resonances of a twisted plasmonic array pair, J. Phys. Chem. C **125**, 25670 (2021).

[80] Y. Zhang, Z. Che, W. Liu, J. Wang, M. Zhao, F. Guan, X. Liu, L. Shi, and J. Zi, Unfolded band structures of photonic quasicrystals and moiré superlattices, Phys. Rev. B **105**, 165304 (2022).

[81] L. Huang, W. Zhang, and X. Zhang, Moiré Quasibound States in the Continuum, Phys. Rev. Lett. **128**, 253901 (2022).

[82] J. Chen, X. Lin, M. Chen, T. Low, H. Chen, and S. Dai, A perspective of twisted photonic structures, Appl. Phys. Lett. **119**, 240501 (2021).

[83] G. Hu, C.-W. Qiu, and A. Alù, Twistronics for photons: Opinion, Opt. Mater. Express **11**, 1377 (2021).

[84] S. G. Tikhodeev, A. L. Yablonskii, E. A. Muljarov, N. A. Gippius, and T. Ishihara, Quasiguided modes and optical prop-erties of photonic crystal slabs, Phys. Rev. B **66**, 045102 (2002).

[85] M. Moharam, E. B. Grann, D. A. Pommet, and T. Gaylord, Formulation for stable and efficient implementation of the rigorous coupled-wave analysis of binary gratings, J. Opt. Soc. Am. A **12**, 1068 (1995).

[86] D. M. Whittaker and I. S. Culshaw, Scattering-matrix treatment of patterned multilayer photonic structures, Phys. Rev. B **60**, 2610 (1999).

[87] S. V. Lobanov, T. Weiss, D. Dregely, H. Giessen, N. A. Gippius, and S. G. Tikhodeev, Emission properties of an oscillating point dipole from a gold Yagi-Uda nanoantenna array, Phys. Rev. B **85**, 155137 (2012).

[88] S. A. Dyakov, N. A. Gippius, I. M. Fradkin, and S. G. Tikhodeev, Vertical Routing of Spinning-Dipole Radiation from a Chiral Metasurface, Phys. Rev. Appl. **14**, 024090 (2020).